Interference and nonlinear properties of four-wave-mixing resonances in thermal vapor: Analytical results and experimental verification

Michał Parniak* and Wojciech Wasilewski
Institute of Experimental Physics, University of Warsaw, Pasteura 5, 02-093 Warsaw, Poland
(Received 23 December 2014; published 17 February 2015)

We develop a model to calculate nonlinear polarization in a nondegenerate four-wave mixing in diamond configuration which includes the effects of hyperfine structure and Doppler broadening. We verify the model against the experiment with $5\,^2S_{1/2}$, $5\,^2P_{3/2}$, $5\,^2D_{3/2}$, and $5\,^2P_{1/2}$ levels of rubidium 85. Treating the multilevel atomic system as a combination of many four-level systems we are able to express the nonlinear susceptibility of a thermal ensemble in a low-intensity regime in terms of Voigt-type profiles and obtain an excellent conformity of theory and experiment within this complex system. The agreement is also satisfactory at high intensity and the analytical model correctly predicts the positions and shapes of resonances. Our results elucidate the physics of coherent interaction of light with atoms involving higher excited levels in vapors at room temperature, which is used in an increasing range of applications.

DOI: 10.1103/PhysRevA.91.023418 PACS number(s): 32.80.Wr, 32.80.Qk, 42.50.Gy, 42.65.Ky

I. INTRODUCTION

Coherent interactions of light and atomic vapors involving higher excited states have attracted much attention recently. A seminal work by Peyronel *et al.* [1] demonstrated electromagnetically induced transparency resonance with extreme single-photon sensitivity due to utilization of Rydberg levels. A host of other works explore the use of multiphoton transitions involving higher states in the context of nonlinear optics and quantum information.

The so-called diamond configuration of atomic levels, as sketched in Fig. 1, is frequently used. Applications include coherent interaction of atoms with ultrashort laser pulses, useful for interferometric measurements [2], and coherent control [3]. In the continuous-wave regime, atoms in diamond configuration demonstrate high resonant nonlinearities that enable generation of coherent blue and infrared light [4–7] via four-wave mixing (4WM), as well as strong phase-dependent response [8]. This up-conversion scheme also enables coherent transfer of light angular momentum [9].

Atoms in diamond configuration have been successfully used as a nonlinear frequency conversion medium [10–13], applicable to light at single-photon level. Both spectral [14,15] and temporal [16] properties of the diamond configuration have been studied. When the diamond configuration involved a Rydberg state, 4WM has also been observed [17] and coherent revival effects have been seen even in a warm ensemble of atoms [18]. A similar configuration is also proposed to be a room-temperature single-photon source [19]. Finally, 4WM in diamond configuration has been used as a source of single-photon pairs [20,21] with well-defined temporal properties [22] which, thanks to proper postselection, can be perfectly matched to absorption by single atoms [23].

In most of the aforementioned works, a maximally five-level-atom model was used to model the experiment. Thereby the interferences between different paths through rich hyperfine structure of actual atoms were neglected. The hyperfine structure inevitably influences any room-temperature experiments where different transitions are driven in classes of atoms depending on their velocity. The susceptibility of a room-temperature ensemble is a convolution of respective cold-atomic function in a multidimensional space of frequencies of the driving fields with a Gaussian corresponding to thermal velocity distribution. This particular convolution reshapes resonances and forms band structures which extend in certain directions while they stay sub-Doppler in others. It is therefore very important to take into account contributions of all hyperfine states or, in other words, a multitude of paths through intermediate levels.

In this paper, we develop simple theoretical tools for predicting the influence of this effect on a coherent process in which it is crucial to consider interference between contributions of different atomic states. We introduce a formalism that enables us to treat the realistic atom as a combination of many four-level atoms. This can be understood as an interference of many possible paths of 4WM. For weak driving fields, the final result is a superposition of Voigt-type profiles, and a relatively simple recipe is provided for higher intensities. The simplicity worked out enables us to explain the intricacies of interference between contributions of various hyperfine sublevels, taking into account the Doppler broadening in a precise and exact way.

We verify our results against experiment in which we measure the intensity of 4WM in diamond configuration in warm rubidium 85 vapor as a function of laser frequencies. The comparison covers both low- and high-intensity regimes. We obtain good conformity of theory and experiment despite complexity of the system.

The effects we describe and explain herein are especially important to studying phase-dependent interactions [2,3,8], to optimizing single-photon generation setups [21,22], and to explaining 4WM spectra observed in many experiments [7,14,15] or possible magnetic field effects.

This paper is organized as follows. In Sec. II, we introduce a theoretical description of 4WM in an inhomogeneously broadened multilevel atomic medium. In Sec. III, we describe the details of our 4WM experiment in rubidium vapors. Section IV presents a comparison of experimental and theoretical data. Section V concludes the paper.

*michal.parniak@fuw.edu.pl

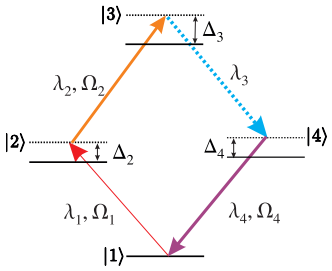

FIG. 1. (Color online) The diamond scheme of atomic levels and transitions. Rubidium 85 is used to generate light at the wavelength $\lambda_3 = 762$ nm via 4WM of incident light fields at the wavelengths $\lambda_1 = 780$ nm, $\lambda_2 = 776$ nm, and $\lambda_4 = 795$ nm, and Rabi frequencies Ω_1, Ω_2, and Ω_4. Levels $|1\rangle$ to $|4\rangle$ correspond to $5\,^2S_{1/2}$, $5\,^2P_{3/2}$, $5\,^2D_{3/2}$, and $5\,^2P_{1/2}$ states of rubidium 85, respectively. The optical frequencies are parametrized by two one-photon detunings Δ_2 and Δ_4 and a two-photon detuning Δ_3. Note that the single-photon detuning of the Ω_2 field can be written as $\Delta_3 - \Delta_2$.

II. THEORY

In this section, we calculate the intensity of the light generated by 4WM in diamond configuration depicted in Fig. 1. We start with calculating the optical coherence in a four-level-atom model. Next, we take into account the hyperfine structure, and finally the Doppler broadening.

A. Nonlinear polarization of a four-level atom

In the experiment we observe the intensity of light generated at the transition between levels $|3\rangle$ and $|4\rangle$ at $\lambda_3 = 762$ nm via 4WM. The starting point for the theoretical treatment is the calculation of steady-state optical coherence ρ_{43} in a four-level atom in diamond configuration. For the sake of simplicity, we assume that the intensity of the incident laser light remains constant along the atomic medium. When the geometry of the laser beams enables perfect wave-vector matching, the amplitude of the emitted light wave E_3 is proportional to the optical polarization P_3, which, in turn, is proportional to the density of atoms n, the dipole moment of the transition μ_{43}^*, and the optical coherence

$$E_3 \propto P_3 = n\mu_{43}^*\rho_{43} + \text{c.c.} \tag{1}$$

The steady-state coherence ρ_{43} can be calculated from the Liouville equation with relaxation, constructed as in Ref. [17]. For low-light intensities, we may use the lowest nonvanishing order of the perturbative solution and obtain a compact formula for the optical coherence:

$$\rho_{43} = \frac{\Omega_1\Omega_2\Omega_4^*}{8\tilde{\Delta}_2\tilde{\Delta}_3\tilde{\Delta}_4^*}, \tag{2}$$

where $\tilde{\Delta}_j = \Delta_j + i\Gamma_j/2$ is the complex detuning of field from level $|j\rangle$, Γ_j is the decay rate of level $|j\rangle$, Ω_k is the Rabi frequency of field E_k coupled to $|k\rangle - |k+1\rangle$ transition for $k = 1,2$, and Ω_4 is the Rabi frequency of field E_4 coupled to $|1\rangle - |4\rangle$ transition, in accordance with Fig. 1. For rubidium 85, the decay rates are $\Gamma_2 = 6.1 \times 2\pi$ MHz, $\Gamma_3 = 0.66 \times 2\pi$ MHz, and $\Gamma_4 = 5.7 \times 2\pi$ MHz. This leads to the following

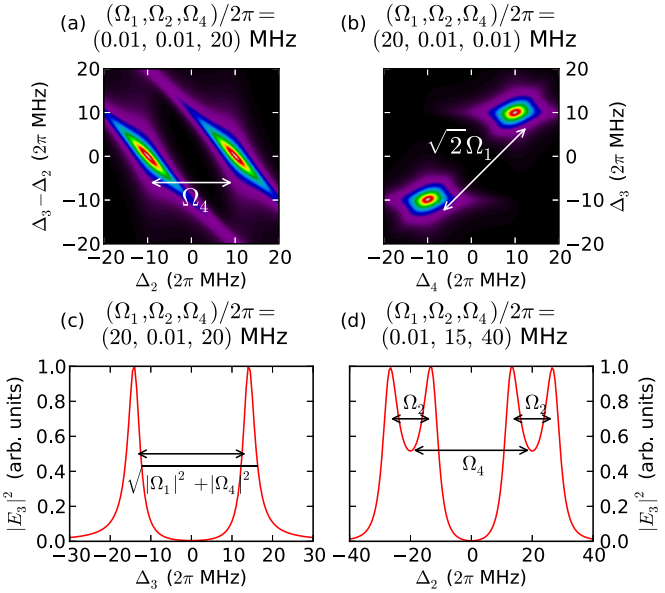

FIG. 2. (Color online) Intensity of the 4WM signal $|E_3|^2$: (a) the detuning of strong Ω_4 driving field is kept constant ($\Delta_4 = 0$) while the frequencies of the Ω_1 field (Δ_2 detuning) and Ω_2 field ($\Delta_3 - \Delta_2$ detuning) are swept to probe the splitting, (b) the detuning of Ω_1 field is kept constant ($\Delta_2 = 0$) while the frequencies of Ω_2 (Δ_3) and Ω_4 (Δ_4) fields are swept, (c) two strong driving fields (Ω_1 and Ω_4) of constant frequency ($\Delta_2 = 0$ and $\Delta_4 = 0$) induce a splitting of $\sqrt{|\Omega_1|^2 + |\Omega_4|^2}$, which is probed by a weak Ω_2 field detuned by Δ_3 from resonance, (d) strong Ω_2 field of constant single-photon detuning from the $|2\rangle - |3\rangle$ resonance ($\Delta_3 = \Delta_2$), and strong Ω_4 field ($\Delta_4 = 0$) causes four peaks to appear when Δ_2 detuning is varied.

expression for the optical polarization:

$$P_3 = n\frac{\mu_{12}\mu_{23}\mu_{43}^*\mu_{14}^*}{8\hbar^3\tilde{\Delta}_2\tilde{\Delta}_3\tilde{\Delta}_4^*}E_1E_2E_4^* + \text{c.c.} \tag{3}$$

For driving light intensities exceeding saturation $\Omega \gtrsim \Gamma$ we need to solve the Liouville equation exactly. A computer algebra system provides an exact solution in the form of a rational function of complex detunings $\tilde{\Delta}_i$ and Rabi frequencies Ω_i. We state this solution in a general way:

$$\rho_{43} = \rho_{43}(\tilde{\Delta}_2, \tilde{\Delta}_3, \tilde{\Delta}_4^*, \Omega_1, \Omega_2, \Omega_4^*). \tag{4}$$

In Fig. 2, we plot the 4WM signal intensity $|E_3|^2$ in various situations, calculated using the solution (4) in Eq. (1), to illustrate an already complex behavior of the system. For high Rabi frequencies, i.e., $\Omega \gtrsim \Gamma$, the system reveals Autler-Townes splitting [15,24] observed in the emission of the signal field. To directly observe the splitting, we set one driving field to be strong [$\Omega_4/2\pi = 20$ MHz in Fig. 2(a) and $\Omega_1/2\pi = 20$ MHz in Fig. 2(b)], while frequencies of the remaining weak fields are swept to probe the structure. In both cases, we see two resonances of the signal field, and their separation is proportional to the strong field Rabi frequency. Even more complex behavior, that can be understood as double dressing of atomic states [25], reveals itself when two of the driving fields are strong. In Fig. 2(c), we set $\Omega_1/2\pi = 20$ MHz and $\Omega_4/2\pi = 20$ MHz. When the two-photon detuning Δ_3 is changed, we observe resonances

separated by $\sqrt{|\Omega_1|^2+|\Omega_4|^2}$. Finally, following [13], we set $\Omega_2/2\pi = 15$ MHz and $\Omega_4/2\pi = 40$ MHz and observe four distinct resonances of four-wave mixing in Fig. 2(d), arising due to double Autler-Townes splitting.

The above solutions can be readily applied to describe 4WM in a cold ensemble of atoms or a single atom where the hyperfine structure of each of the intermediate levels is fully resolved. Even though these solutions can already be quite complex, they do not provide significant insight into the behavior of the Doppler broadened medium, where direct observation of Autler-Townes splitting becomes harder.

B. Hyperfine structure: Interference of paths

In order to fully account for the hyperfine structure of a real atom, we would have to solve the Liouville equation for an excessively large density matrix. Later in this paper, we deal with an experimental case where the equation would have to take into account at least 64 atomic states. Solution of the resulting steady-state Liouville equation for a range of parameters, such as detunings would be hard to compute. Instead, we propose an alternative solution to this problem that can be computed much more rapidly. For the sake of simplicity, we assume that all light fields, both the driving ones and the signal one, have a fixed polarization parallel to the quantization axis x, as this is our experimental situation.

In our method, we treat the full system as a set of many four-level systems. Each of these can be represented as a certain path $\mathcal{P} = \{|F_1\, m_{F_1}\rangle, |F_2\, m_{F_2}\rangle, |F_3\, m_{F_3}\rangle, |F_4\, m_{F_4}\rangle, |F_1\, m_{F_1}\rangle\}$, through intermediate levels, where F_i is the total angular momentum of the state $|i\rangle$, and m_{F_i} is its projection. As a path $\mathcal{P}$ we understand a list of five atomic states. Each state belongs to the hyperfine manifold of appropriate level $|1\rangle$ to $|4\rangle$ and is characterized by a specific F and m_F for a given path. Each path can be characterized by different dipole moments $\mu_{ij}(\mathcal{P})$, and different hyperfine detunings $\Delta_i(\mathcal{P})$. Angular momenta for all of the excited levels $|2\rangle$, $|3\rangle$, and $|4\rangle$ vary through all possible values, but for the ground state $|1\rangle$, which is both the initial and the final state of the path, we choose only one ground-state angular momentum F_1 and vary only its projection m_{F_1}. This is due to the fact that the ground-state hyperfine manifold is fully resolved in our experimental case.

The dipole moments $\mu_{ij}(\mathcal{P}) = \langle J_i \mathcal{I}\, F_i m_{F_i}|\hat{\mu}|J_j \mathcal{I} F_j m_{F_j}\rangle$, where $\hat{\mu}$ is the dipole moment operator, $\mathcal{I}$ is the nuclear spin, and J_i is the total angular momentum of the electron on the level $|i\rangle$, are calculated using known values of reduced dipole moments $\mu_{ij} = \langle J_i||\hat{\mu}||J_j\rangle$ according to the formulas given in Ref. [26]. The complex detunings $\tilde{\Delta}_i(\mathcal{P})$ calculated from respective lines are affected by hyperfine shifts in the following way:

$$\tilde{\Delta}_i(\mathcal{P}) = \tilde{\Delta}_i + \Delta F_i - \Delta F_1, \tag{5}$$

where ΔF_i is the shift of a given F_i from the centroid of the manifold $|i\rangle$. It follows that the detunings $\tilde{\Delta}_i$ are measured to the manifold centroids.

In our experimental case, 61 paths through intermediate states contribute to the optical polarization P_3. For each path $\mathcal{P}$ we calculate its contribution $P_3(\mathcal{P})$ by inserting solution (4) into Eq. (1). In total, we obtain

$$P_3 = \sum_{\mathcal{P}} n(\mathcal{P})\mu_{43}^*(\mathcal{P})\rho_{43}(\mathcal{P}) + \text{c.c.}, \tag{6}$$

where $n(\mathcal{P})$ is the density of the atoms in the ground-state sublevel F_1, m_{F_1} of a particular path $\mathcal{P}$, while $\rho_{43}(\mathcal{P})$ is calculated taking into account hyperfine shifts and dipole moments corresponding to the given path $\mathcal{P}$. The above equation expresses an approximation neglecting coherent interplay of different paths in a single atom.

However, such interplays may only matter when two paths share common levels and some coherences oscillate at similar frequencies. In our experimental situation, all of the optical fields are polarized linearly in the same direction x, which we take as quantization axis. In this case, all m_{F_i} in each path are the same due to selection rules for dipole moments. Consequently, if two distinct paths share a level $|i\rangle$, then they must have a different total angular momentum F_j at some other level $|j\rangle$. The natural oscillation frequencies of coherences for these paths differ by the hyperfine splitting. As the Rabi frequencies in our experiment are smaller than the hyperfine splittings, we conjecture such paths will not interplay coherently. This is verified in the experiment. Strong driving beams significantly redistribute the atoms among the ground-state sublevels F_1, m_{F_1} altering $n(\mathcal{P})$. We find the steady state of a set of rate equations to determine $n(\mathcal{P})$ and thus the relative contributions of paths.

To conclude this section, let us note that within the limit of low intensities of driving fields $\Omega \ll \Gamma$, the total polarization can be calculated exactly using perturbation calculus. In the lowest nonvanishing order, Eq. (3) can be inserted into Eq. (6) leading to a simple result:

$$P_3 = \epsilon_0 E_1 E_2 E_4^* \sum_{\mathcal{P}} \chi(\mathcal{P}) + \text{c.c.}, \tag{7}$$

where we identified the susceptibility $\chi(\mathcal{P})$ of the system:

$$\chi(\mathcal{P}) = n(\mathcal{P}) \frac{\mu_{12}(\mathcal{P})\mu_{23}(\mathcal{P})\mu_{43}^*(\mathcal{P})\mu_{14}^*(\mathcal{P})}{8\epsilon_0\hbar^3 \tilde{\Delta}_2(\mathcal{P})\tilde{\Delta}_3(\mathcal{P})\tilde{\Delta}_4^*(\mathcal{P})}. \tag{8}$$

The above expression approximates the rough features of full nonperturbative solution quite well and we find it worthwhile to track the contributions of various hyperfine components to the final result. We list them in Table I for the 4WM process we study in experiment.

TABLE I. Theoretical relative amplitudes of 4WM resonances in rubidium 85 (F_3 ground state) parametrized by spin of $|2\rangle$ and $|4\rangle$ states F_2 and F_4 for each spin projection of the ground state m_{F_1}. The result is summed over the spin of highest excited state $F_3 = 1 \ldots 4$ due to negligible hyperfine splitting.

$\chi(\mathcal{P})$	$F_2=2$				$F_2=3$				$F_2=4$			
$\lvert m_{F_1}\rvert$	3	2	1	0	3	2	1	0	3	2	1	0
$F_4=2$	0	−40	32	72	0	140	56	0	0	180	360	432
$F_4=3$	0	80	32	0	360	0	−21	0	216	144	45	0

C. Doppler broadening

The final step in the construction of our model consists in averaging the contributions of atoms moving with various velocities v along almost parallel laser beams. We take the one-dimensional Maxwell-Boltzmann velocity distribution $g(v) = \sqrt{\frac{m}{2\pi k_B T}}\exp(-\frac{mv^2}{2k_B T})$, where m is the atomic mass, T is the temperature, and k_B is the Boltzmann's constant, to calculate the number of atoms with velocity v. To perform the average over the thermal ensemble, we introduce velocity-dependent detunings: $\tilde{\Delta}_2^{(v)} = \tilde{\Delta}_2 + \frac{2\pi v}{\lambda_1}$, $\tilde{\Delta}_3^{(v)} = \tilde{\Delta}_3 + \frac{2\pi v}{\lambda_1} + \frac{2\pi v}{\lambda_2}$, $\tilde{\Delta}_4^{(v)} = \tilde{\Delta}_4 + \frac{2\pi v}{\lambda_4}$. Then, we integrate the optical polarization P_3 with the velocity distribution $g(v)$, obtaining

$$\langle P_3\rangle_T = \int_{-\infty}^{+\infty}\sum_{\mathcal{P}} g(v)n(\mathcal{P})\mu_{43}^*(\mathcal{P})\rho_{43}(\mathcal{P},v)dv + \text{c.c.}, \quad (9)$$

where we have neglected velocity-dependent pumping effects and assumed the distribution of the atoms among ground levels $n(\mathcal{P})$ to be velocity independent.

In the perturbative case $\Omega \ll \Gamma$, we can perform the above integration analytically. Since only the susceptibility $\chi(\mathcal{P})$ given in Eq. (8) is velocity dependent, the velocity-averaged version of Eq. (7) is $\langle P_3\rangle_T = \epsilon_0 E_1 E_2 E_4^* \sum_{\mathcal{P}}\langle\chi(\mathcal{P})\rangle_T + \text{c.c.}$ Here, the susceptibility $\langle\chi(\mathcal{P})\rangle_T$ is calculated by integrating $g(v)/\tilde{\Delta}_2^{(v)}\tilde{\Delta}_3^{(v)}\tilde{\Delta}_4^{(v)*}$, which in turn is reduced into a sum of Voigt-type profile integrals. This is achieved by partial fractions decomposition as detailed in the Appendix. The result can be cast into the following form:

$$\langle\chi(\mathcal{P})\rangle_T = n(\mathcal{P})\frac{\mu_{12}(\mathcal{P})\mu_{23}(\mathcal{P})\mu_{43}^*(\mathcal{P})\mu_{14}^*(\mathcal{P})}{16i\epsilon_0\hbar^3} \times\sqrt{\frac{m}{2\pi k_B T}}\sum_i \frac{\Lambda_i \mathcal{V}\left[\tilde{\Delta}_i(\mathcal{P})\frac{\Lambda_i}{2\pi}\sqrt{\frac{k_B T}{2m}}\right]}{Q_i[\{\tilde{\Delta}_j(\mathcal{P})\}]}, \quad (10)$$

where $\mathcal{V}(z)$ is the profile function we define in the Appendix, $\Lambda_2 = \lambda_1$, $\Lambda_3 = \frac{\lambda_1\lambda_2}{\lambda_1+\lambda_2}$, $\Lambda_4 = \lambda_4$ and $Q_i(\{\tilde{\Delta}_j\})$ are second-order polynomials of detunings. The polynomials $Q_i(\{\tilde{\Delta}_j\})$, given in the Appendix as well, are responsible for the sub-Doppler features in the 4WM spectrum. Their real parts are zero when real parts of any two out of three factors in the susceptibility denominator $\tilde{\Delta}_2^{(v)}\tilde{\Delta}_3^{(v)}\tilde{\Delta}_4^{(v)*}$ are zero for the same velocity v. This determines the position of the resonances, as we will see in Sec. IV.

III. EXPERIMENT

The heart of the experimental setup is a magnetically shielded rubidium vapor cell heated to the temperature of 373 K. The 2.5-cm-diameter and 7.5-cm-long cell contains a natural mixture of rubidium isotopes and no buffer gas. We have decided to use only ^{85}Rb (nuclear spin $\mathcal{I} = \frac{5}{2}$) due to its higher concentration and, in consequence, higher optical depth. For the ground state $|1\rangle$ we have chosen the $F_1 = 3$ hyperfine component of the $5\,^2S_{1/2}$ state. For the intermediate states, we have chosen $5\,^2P_{3/2}$ for the $|2\rangle$ state and $5\,^2P_{1/2}$ for the last intermediate state $|4\rangle$. As the highest excited state $|3\rangle$ we use the $5\,^2D_{3/2}$ level. The respective wavelengths for the resonant transitions are $\lambda_1 = 780$ nm (the D2 line),

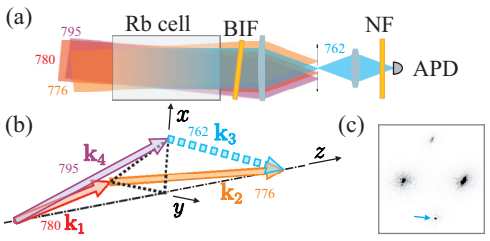

FIG. 3. (Color online) Schematic of the experimental situation. Generation and detection stage (a) of the experimental setup; beams enter the rubidium vapor cell and the four-wave-mixing signal is separated from the driving light using spatial separation, bandpass interference (BIF) filter, and a notch filter (NF). The signal is detected using an avalanche photodiode (APD). The 3D configuration of beams (b) enables phase matching without beam overlap. In the focal plane (c) we see four distinct points corresponding to four beams. The signal at 762 nm is marked with an arrow.

$\lambda_2 = 776$ nm, $\lambda_3 = 762$ nm, and $\lambda_4 = 795$ nm (the D1 line). Out of many possible diamond configurations, the one we use has the main advantage of high efficiency of detectors for each of the wavelengths, thus enabling future quantum optics applications.

Inside the cell, three beams from three different lasers at 780, 795, and 776 nm intersect at a small angle as depicted in Fig. 3. The fourth beam of light at 762 nm is generated in the cell according to the phase-matching condition $\mathbf{k_1} + \mathbf{k_2} = \mathbf{k_3} + \mathbf{k_4}$. The values of wave vectors are approximately $\mathbf{k_1} \approx \frac{2\pi}{\lambda_1}[0,-\theta,1]$, $\mathbf{k_2} \approx \frac{2\pi}{\lambda_2}[0,\theta,1]$, $\mathbf{k_3} \approx \frac{2\pi}{\lambda_3}[-\theta,0,1]$, and $\mathbf{k_4} \approx \frac{2\pi}{\lambda_4}[\theta,0,1]$, where $\theta = 8$ mrad. The nearly collinear configuration entails broad phase matching. Experimentally, we verified that varying the angle of $\mathbf{k_1}$ by 2 mrad shifts the signal beam accordingly but does not have significant influence on signal intensity. Inside the cell, the beams are collimated with a $1/e^2$ diameter of approximately 3 mm.

We use three Toptica lasers: two distributed feedback diodes at 780 and 795 nm and an external cavity laser at 776 nm. The beams are combined to intersect at a small angle inside the cell and then we employ a high-extinction Wollaston polarizer to prepare the light of all beams in the x polarization state.

Finally, the generated 762-nm light needs to be separated from the driving beams. We use three distinct filtering methods to obtain high signal-to-background ratio, as shown in Fig. 3(c). A tilted interference bandpass filter comes first, then we use an iris diaphragm in the focal plane to cover the driving beams, and finally we apply a notch filter with a central wavelength of 785 nm (Thorlabs NF785-33). The only residual light from the driving lasers we detect comes from the amplified spontaneous emission at 762 nm in laser diodes. The 4WM signal is detected using an avalanche photodiode (Thorlabs APD120A).

The measurement scheme is designed to obtain maps of the 4WM signal as a function of two out of three driving laser detunings. We lock the frequency of the 776-nm laser using a wavelength meter (Angstrom WS-7) at a fixed detuning Δ_{776}, nearly resonant to the $|2\rangle - |3\rangle$ transition. During the measurement, the detuning Δ_{795} of the 795-nm laser frequency is altered in small steps of $4 \times 2\pi$ MHz, while the detuning Δ_{780} of the 780-nm laser is scanned over the relevant range

of optical frequencies. The exact scan rate varied for different measurements, but was of the order of $50 \times 2\pi$ MHz/ms. Data from 800 to 1000 scans were collected and averaged to give a dependence of the 4WM signal from Δ_{780} for fixed Δ_{795} and Δ_{776}.

All detunings are measured from the centroid of respective resonance line. The detunings of lasers resonant to D1 and D2 lines are determined using saturated absorption signal obtained in auxiliary rubidium vapor cells. Note that through comparing the laser detunings with the theoretical model, we obtain $\Delta_2 = \Delta_{780}$, $\Delta_3 = \Delta_{780} + \Delta_{776}$, and $\Delta_4 = \Delta_{795}$.

IV. RESULTS

The first measurement we present was aimed to determine the shape of a single 4WM resonance in the regime of a perturbative solution. To verify the linear perturbative theory we performed a measurement of the 4WM signal, where all driving field intensities were low and corresponded to the Rabi frequencies of $\Omega_1/2\pi = 5$ MHz, $\Omega_2/2\pi = 0.3$ MHz, and $\Omega_4/2\pi = 4$ MHz. Note that these are all lower than corresponding transitions' linewidths. We chose the strongest resonance that corresponded to the path leading through $F_2 = 4$, $F_3 = 3$, and then $F_4 = 2$ levels. The choice of such a configuration entails that there should be no splitting of this resonance due to the hyperfine structure of the highest $|3\rangle$ state, as there is only one possible spin F_3 if $F_2 = 4$ and $F_4 = 2$.

Figures 4(a) and 4(b) present the experimental and theoretical 4WM signal intensity $|E_3|^2$, respectively. The presented maps show an excellent conformity of theory [Eq. (10)] and experiment. The only free parameter for the theory is the intensity multiplicative factor. Additionally, we need to take into account the laser linewidth, which is of the order of several MHz for each laser when averaged over duration of a single measurement.

In Figs. 4(c) and 4(d), we present two cross sections of the maps. The cross sections, denoted by dashed lines on the maps, are taken far from the resonance, as the structure there is nontrivial. It exhibits two peaks and it is instructive to observe their separation and relative intensities. The cross sections show a quantitative agreement between theory (solid line) and experiment (dots with error bars), confirming the correctness of our theoretical approach. On the maps we observe a small discrepancy of intensity and shape in the very center of the resonance that are due to small nonlinearity, as the Rabi frequencies are only slightly lower than the linewidths.

The results of the second measurement we present here demonstrate the influence of the hyperfine structure of intermediate levels on the 4WM signal. For this measurement we increased the power of each of the driving lasers, and obtained Rabi frequencies of $\Omega_1/2\pi = 34$ MHz, $\Omega_2/2\pi = 0.7$ MHz, and $\Omega_4/2\pi = 28$ MHz. As the ground state is the $F_1 = 3$ state, we expect six possible resonances, as this ground state is coupled to three hyperfine levels ($F_2 = 2,3,4$) of the $|2\rangle$ state and two hyperfine levels ($F_4 = 2,3$) of the $|4\rangle$ state. We do not expect to see different resonances arising due to the hyperfine structure of the highest state $|3\rangle$, as the hyperfine splitting of this state is smaller than the resolution of our experiment.

Figures 5(a) and 5(b) present the experimental and theoretical results for the 4WM signal, respectively. We identify the

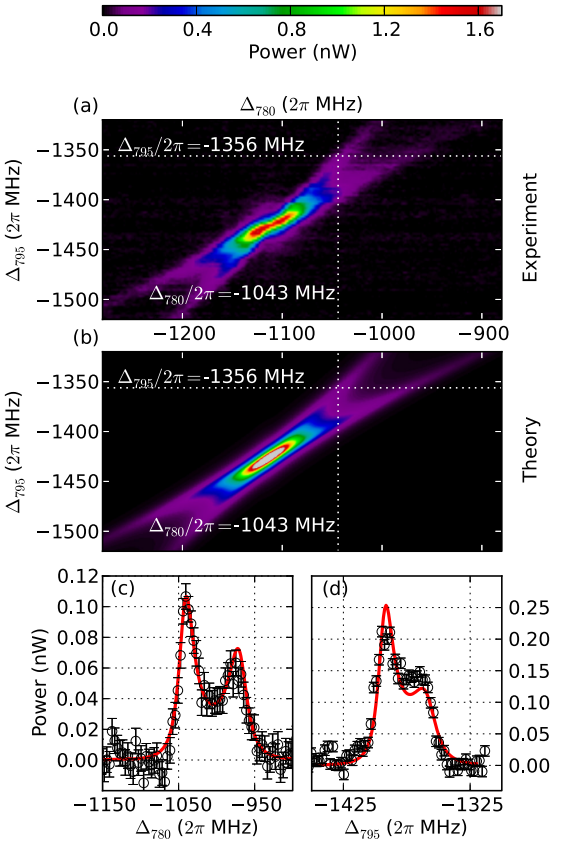

FIG. 4. (Color online) Experimental (a) and theoretical (b) maps of the intensity of the 4WM signal $|E_3|^2$ as a function of 780- and 795-nm laser detunings in case of low driving field intensities around the $F_2 = 2$ and $F_4 = 4$ resonance. The cross sections, marked on the maps with dashed lines, from experimental (dots with error bars) and theoretical (solid lines) data are presented in figures (c) and (d), where (c) depicts the horizontal and (d) the vertical cross section. The detuning of the 776-nm laser frequency was $\Delta_{776}/2\pi = -51$ MHz.

positions of the resonances corresponding to the crossings of the dashed lines. Each line corresponds to a certain hyperfine level of the $|2\rangle$ or the $|4\rangle$ state; these lines correspond to zeros of the real part of denominator of Eq. (10), or more precisely the polynomials L_{ij}, defined in the Appendix. This brings about two resonance conditions

$$\Delta_{780} = -\Delta F_1 + \frac{\lambda_1 + \lambda_2}{\lambda_1}\Delta F_2 + \frac{\lambda_1}{\lambda_2}\Delta_{776}, \tag{11}$$

$$\Delta_{795} = \frac{\lambda_1\lambda_2}{(\lambda_1 + \lambda_2)\lambda_4}(\Delta_{780} + \Delta_{776}) + \left(\frac{\lambda_1\lambda_2}{(\lambda_1 + \lambda_2)\lambda_4} - 1\right)\Delta F_1 + \Delta F_4, \tag{12}$$

where again we neglected hyperfine splitting of the highest excited state $|3\rangle$. The first equation defines the lines corresponding to hyperfine levels of the $|2\rangle$ state. These are vertical on our map, but their separation is twice the hyperfine splitting, as $\frac{\lambda_1+\lambda_2}{\lambda_1} \approx 2$. The second equation defines the lines corresponding to the $|4\rangle$ state. These lines have a slope of $\frac{\lambda_1\lambda_2}{(\lambda_1+\lambda_2)\lambda_4} \approx \frac{1}{2}$, but their separation is simply equal to the splitting of the $|4\rangle$ state.

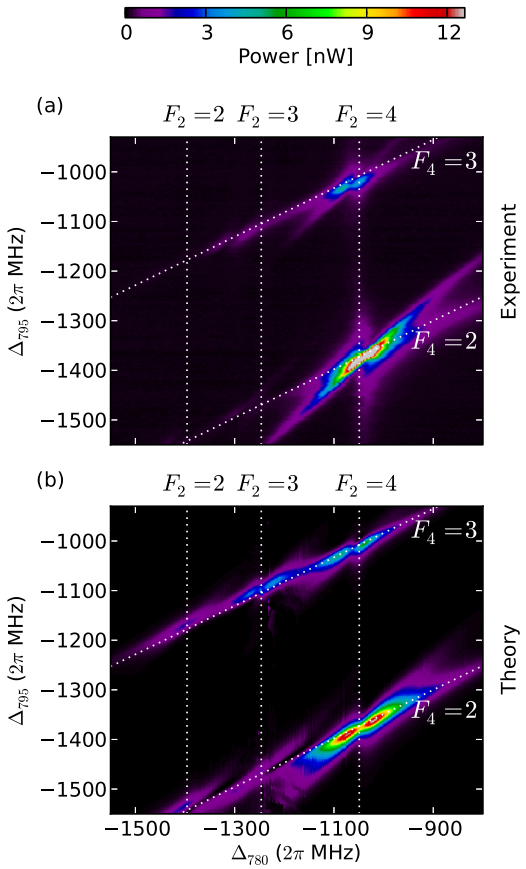

FIG. 5. (Color online) Experimental (a) and theoretical (b) 4WM signal demonstrating all possible resonances arising due to the hyperfine structure. Dashed lines correspond to the resonance conditions given by Eqs. (11) and (12) for different F_2 and F_4. Crossings of the lines correspond the four-wave-mixing resonances. The detuning of the 776-nm laser frequency was $\Delta_{776}/2\pi = 30$ MHz.

For the full theoretical calculation [Fig. 5(b)], we use the nonperturbative framework introduced in Sec. II. The results show good qualitative agreement with the experiment. We observe that both in theory and experiment, the strongest resonances are the rightmost ones on our map, corresponding to highest F_2 spin. This is due to the relative amplitudes of resonances, that can be calculated even in the perturbative regime from the products of dipole moments. In Table I, we give these relative amplitudes for each resonance as a function of the ground-state spin projection $|m_{F_1}|$. Note that different ground-state populations give rise to different 4WM resonances. Consequently, nonequilibrium populations may significantly change observed relative amplitudes. In our calculation, we take this into account by modifying ground-state populations according to the numerical solution of Liouville equation with relaxation and repopulation [27].

One of the nonlinear effects we predict theoretically and observe experimentally is Autler-Townes–type splitting [15,24] of the $F_2 = 4$, $F_4 = 3$ resonance, that does not occur in the linear regime. Another effect observed near the $F_2 = 4$, $F_4 = 2$ resonance is bending of the resonance line towards the vertical direction. Namely, we note relatively higher intensity as compared to the linear case in the top-left and bottom-right corners of the resonance.

In the experiment, we witness two more effects that are not present in the theoretical results. The first effect is that the leftmost resonances, corresponding to lowest F_2 spin values, are even less intense than predicted. The second effect is the appearance of narrow diagonal lines in the 4WM signal, which should be less intense according to our theory. We believe that these two effects stem from velocity-selective optical pumping, that our model does not take into account at all. Nevertheless, we find the agreement between our theoretical and experimental results satisfactory.

V. CONCLUSIONS

Beginning with the theoretical description of a four-level atom, we have derived a model for the the intensity of 4WM in a multilevel atomic medium with inhomogeneous broadening. We are able to take into account the interference of many possible paths of 4WM with a simple formalism, that could be easily extended to many similar situations, including possibly higher-order transitions. Our model is a reasonable compromise between simplicity and accuracy for predicting intensities, shapes, and positions of 4WM resonances.

In the experimental part, we have demonstrated the influence of the rich level structure of rubidium on the 4WM process. We have obtained excellent agreement between theory and experiment for low driving field intensities, as well as good qualitative agreement for higher driving field intensities, where more nonlinear processes contribute.

Combined with optical pumping, our methods may facilitate the design of coherent control in a multilevel atomic medium with light. We have shown that light at 762 nm couples to the population of the ground state. Future investigations could include coupling of 762-nm light to the ground-state coherence in order to create Raman-scattering-like light-atom interface [28] or engineering the 4WM signal by optically pumping the ground state. This could be accomplished in the cells with buffer gas that makes the atomic motion diffusive [29], the cell with antirelaxation coating [30], or in a cold-atomic ensemble. Another approach could involve control of 4WM signal through velocity-selective optical pumping.

ACKNOWLEDGMENTS

We acknowledge the generous support from K. Banaszek, C. Radzewicz, and T. Stacewicz, as well as insightful discussions with R. Chrapkiewicz. This work was supported by the National Science Center Grant No. DEC-2011/03/D/ST2/01941 and by the Polish Ministry of Science and Higher Education "Diamentowy Grant" Project No. DI2013 011943.

APPENDIX: ENSEMBLE-AVERAGED SUSCEPTIBILITY

We decompose the formula (2) for the optical coherence ρ_{43} in the perturbative regime with velocity-dependent detunings, obtaining a sum of three expressions with first-order polynomials in terms of velocity in the denominators:

$$\left(\tilde{\Delta}_2^{(v)}\tilde{\Delta}_3^{(v)}\tilde{\Delta}_4^{(v)*}\right)^{-1} = \sum_i \left[\tilde{\Delta}_i^{(v)} Q_i(\{\tilde{\Delta}_j\})\right]^{-1}. \quad \text{(A1)}$$

The polynomials are $Q_2 = L_{23}L_{24}$, $Q_3 = \frac{\lambda_4(\lambda_1+\lambda_2)^2}{\lambda_1\lambda_2^2}L_{23}L_{34}$, $Q_4 = \frac{\lambda_1}{\lambda_2}L_{24}L_{34}$, where $L_{23} = (1+\frac{\lambda_1}{\lambda_2})\tilde{\Delta}_2 - \tilde{\Delta}_3$, $L_{24} = \frac{\lambda_1}{\lambda_2}\tilde{\Delta}_2 - \tilde{\Delta}_4$, and $L_{34} = \lambda_4(\frac{1}{\lambda_1}+\frac{1}{\lambda_2})\tilde{\Delta}_4 - \tilde{\Delta}_3$. Equating the real part of L_{ij} to zero yields resonance conditions given by Eqs. (11) and (12). The expression can now be easily integrated with velocity distribution $g(v)$, as each component can be integrated separately to give the Voigt-type profile used in Eq. (10):

$$\int_{-\infty}^{\infty}\frac{e^{-v^2/2\langle v^2\rangle}}{2\pi v/\Lambda+\tilde{\Delta}}dv = \frac{\Lambda}{2i}\exp\left[-\frac{\tilde{\Delta}^2\left(\frac{\Lambda}{2\pi}\right)^2}{2\langle v^2\rangle}\right]\left[\operatorname{erf}\left(i\frac{\tilde{\Delta}\frac{\Lambda}{2\pi}}{\sqrt{2\langle v^2\rangle}}\right)\pm 1\right] = \frac{\Lambda}{2i}\mathcal{V}\left(\frac{\tilde{\Delta}\frac{\Lambda}{2\pi}}{\sqrt{2\langle v^2\rangle}}\right), \tag{A2}$$

where we take $+1$ for $\mathrm{Im}(\tilde{\Delta}) > 0$ and -1 otherwise and $\langle v^2\rangle = \frac{k_B T}{m}$. The profile function is defined as

$$\mathcal{V}(z) = \begin{cases} e^{-z^2}[\operatorname{erf}(iz)+1], & \mathrm{Im}(z) > 0 \\ e^{-z^2}[\operatorname{erf}(iz)-1], & \mathrm{Im}(z) < 0. \end{cases} \tag{A3}$$

Note that it is customary to use the Faddeeva function $w(z) = e^{-z^2}[\operatorname{erf}(iz)+1]$ [27], but neither this function nor the plasma dispersion function can be used here, as they would yield incorrect results in the lower half of the complex plane.

[1] T. Peyronel, O. Firstenberg, Q.-Y. Liang, S. Hofferberth, A. V. Gorshkov, T. Pohl, M. D. Lukin, and V. Vuletić, Nature (London) **488**, 57 (2012).

[2] S. Clow and T. Weinacht, Phys. Rev. A **82**, 023411 (2010).

[3] H.-g. Lee, H. Kim, J. Lim, and J. Ahn, Phys. Rev. A **88**, 053427 (2013).

[4] J. F. Sell, M. A. Gearba, B. D. DePaola, and R. J. Knize, Opt. Lett. **39**, 528 (2014).

[5] T. Meijer, J. D. White, B. Smeets, M. Jeppesen, and R. E. Scholten, Opt. Lett. **31**, 1002 (2006).

[6] A. S. Zibrov, M. D. Lukin, L. Hollberg, and M. O. Scully, Phys. Rev. A **65**, 051801 (2002).

[7] A. M. Akulshin, R. J. McLean, A. I. Sidorov, and P. Hannaford, Opt. Express **17**, 22861 (2009).

[8] G. Morigi, S. Franke-Arnold, and G.-L. Oppo, Phys. Rev. A **66**, 053409 (2002).

[9] G. Walker, A. S. Arnold, and S. Franke-Arnold, Phys. Rev. Lett. **108**, 243601 (2012).

[10] T. Chanelière, D. N. Matsukevich, S. D. Jenkins, T. A. B. Kennedy, M. S. Chapman, and A. Kuzmich, Phys. Rev. Lett. **96**, 093604 (2006).

[11] P. S. Donvalkar, V. Venkataraman, S. Clemmen, K. Saha, and A. L. Gaeta, Opt. Lett. **39**, 1557 (2014).

[12] A. G. Radnaev, Y. O. Dudin, R. Zhao, H. H. Jen, S. D. Jenkins, A. Kuzmich, and T. A. B. Kennedy, Nat. Phys. **6**, 894 (2010).

[13] H. H. Jen and T. A. B. Kennedy, Phys. Rev. A **82**, 023815 (2010).

[14] R. T. Willis, F. E. Becerra, L. A. Orozco, and S. L. Rolston, Phys. Rev. A **79**, 033814 (2009).

[15] F. E. Becerra, R. T. Willis, S. L. Rolston, and L. A. Orozco, Phys. Rev. A **78**, 013834 (2008).

[16] F. E. Becerra, R. T. Willis, S. L. Rolston, H. J. Carmichael, and L. A. Orozco, Phys. Rev. A **82**, 043833 (2010).

[17] A. Kölle, G. Epple, H. Kübler, R. Löw, and T. Pfau, Phys. Rev. A **85**, 063821 (2012).

[18] B. Huber, A. Kölle, and T. Pfau, Phys. Rev. A **90**, 053806 (2014).

[19] M. M. Müller, A. Kölle, R. Löw, T. Pfau, T. Calarco, and S. Montangero, Phys. Rev. A **87**, 053412 (2013).

[20] R. T. Willis, F. E. Becerra, L. A. Orozco, and S. L. Rolston, Opt. Express **19**, 14632 (2011).

[21] W. Zhang, D.-S. Ding, J.-S. Pan, and B.-S. Shi, Chin. Phys. Lett. **31**, 064208 (2014).

[22] B. Srivathsan, G. K. Gulati, B. Chng, G. Maslennikov, D. Matsukevich, and C. Kurtsiefer, Phys. Rev. Lett. **111**, 123602 (2013).

[23] G. K. Gulati, B. Srivathsan, B. Chng, A. Cerè, D. Matsukevich, and C. Kurtsiefer, Phys. Rev. A **90**, 033819 (2014).

[24] S. H. Autler and C. H. Townes, Phys. Rev. **100**, 703 (1955).

[25] C. Wei, D. Suter, A. S. M. Windsor, and N. B. Manson, Phys. Rev. A **58**, 2310 (1998).

[26] D. A. Steck, http://steck.us/alkalidata/rubidium85numbers.pdf (Version 2.1.6, last revised 20 Sep. 2013) (unpublished).

[27] W. Happer, Y.-Y. Jau, and T. Walker, *Optically Pumped Atoms* (Wiley, Weinheim, Germany, 2010).

[28] R. Chrapkiewicz and W. Wasilewski, Opt. Express **20**, 29540 (2012).

[29] M. Parniak and W. Wasilewski, Appl. Phys. B **116**, 415 (2014).

[30] M. V. Balabas, K. Jensen, W. Wasilewski, H. Krauter, L. S. Madsen, J. H. Müller, T. Fernholz, and E. S. Polzik, Opt. Express **18**, 5825 (2010).